The break-up of Ekman theory in a flow subjected to background rotation and driven by a non-conservative body force

M. Duran-Matute,[1,a)] G. Di Nitto,[2] R. R. Trieling,[3] L. P. J. Kamp,[3] and G. J. F. van Heijst[3]

[1]*Department of Physical Oceanography, Royal Netherlands Institute for Sea Research, P.O. Box 59, Den Burg (Texel), The Netherlands*

[2]*DICEA, Sapienza Università di Roma, via Eudossiana 18, 00184 Rome, Italy*

[3]*Department of Applied Physics and J. M. Burgerscentre, Eindhoven University of Technology, P.O. Box 513, 5600 MB Eindhoven, The Netherlands*

(Received 9 July 2012; accepted 19 October 2012; published online 28 November 2012)

We present an experimental/numerical study of a dipolar flow structure in a shallow layer of electrolyte driven by electromagnetic forcing and subjected to background rotation. The aim of this study is to determine the influence of a non-conservative body force on the range of applicability of the classical Ekman boundary layer theory in rapidly rotating systems. To address this question, we study the response of the flow to the three control parameters: the magnitude of the forcing, the rotation rate of the system, and the shallowness of the layer. This response is quantified taking into account the magnitude of the flow velocity (represented by the Reynolds number), the symmetry between both vortex cores, and the vertical profile of the horizontal velocity. As in the case without background rotation, the response of the flow exhibits two scaling regimes (a linear and a nonlinear regime) in which the flow exhibits different vertical profiles of velocity. The transition between the two regimes occurs when the convective acceleration becomes of the same order as the viscous damping. This suggests that the applicability of the Ekman theory depends on the existence of a balance between the forcing and the damping due to the Ekman layers and does not depend solely on the value of the Rossby number as for decaying flows. On the other hand, the cyclone/anticyclone asymmetry is governed exclusively by the Rossby number. [http://dx.doi.org/10.1063/1.4766818]

I. INTRODUCTION

Despite their relatively small thickness, Ekman boundary layers play an essential role in the evolution of flows subjected to background rotation since their influence can extend over the whole fluid depth, and hence, they can determine the overall behavior of the flow. The clearest example might be the case of spin-up/down, which is perfectly explained in a simple and elegant way by the Ekman boundary layer theory (see, e.g., Ref. 1). This theory was developed to explain the structure of oceanic and atmospheric boundary layers, and it implies a balance between viscous forces and the Coriolis force within the boundary layer.[2] Commonly, the Ekman layer theory is said to be valid when a geostrophic balance (i.e., a balance between the Coriolis force and the pressure gradient force) exists outside the boundary layer. This is assumed to be the case if the value of the Rossby number, which characterizes the ratio of the magnitude of the convective acceleration to the magnitude of the Coriolis acceleration, is much smaller than unity. In the case

[a)]This research was performed while M. Duran-Matute was at Department of Applied Physics and J. M. Burgerscentre, Eindhoven University of Technology, P.O. Box 513, 5600 MB Eindhoven, The Netherlands. Electronic mail: matias.duran-matute@nioz.nl.

of a decaying monopolar vortex, the Rossby number is associated with the relative thickness of the Ekman boundary layer with respect to that of the boundary layer in the case without background rotation. In this case, the Ekman theory is applicable if the Ekman boundary layer is thicker than the boundary layer for a similar vortex without background rotation.[3]

The fact that the validity of the Ekman theory rests on the existence of simple force balances raises the question of the influence of additional non-conservative body forces (e.g., when electromagnetic or buoyancy forces are present). These type of forces drive flows in different geophysical settings like rotating turbulent convection and magnetohydrodynamic (MHD) flows inside planetary cores, which are strongly dependent on Ekman boundary layer dynamics. For example, King *et al.*[4] have shown experimentally that there is a transition between two different regimes in rotating Rayleigh-Bénard convection when the thermal boundary layer becomes thicker than the Ekman layer, and Kunnen *et al.*[5] have attributed an increase in heat transfer to Ekman pumping.

Both convective and MHD flows subjected to background rotation present very complex dynamics due, in particular, to the fact that the forcing depends on the flow itself. This makes isolating the effect of a simpler non-conservative body force on the Ekman boundary layer difficult. To overcome this difficulty in the current paper, we study a flow in an electrolyte, which is driven by electromagnetic forcing and subjected to background rotation. This particular type of forcing in electrolytes presents several advantages: it is not modified by the flow; its magnitude can be measured easily; its spatial distribution can be computed analytically; and it can be included as a source term in the Navier-Stokes equations (see, e.g., Refs. 6 and 7). These characteristics allow establishing a clear relationship between the forcing and the response of the flow. For example, for a flow similar to the one studied here but without background rotation, the response of the flow to the forcing presents two scaling regimes: a linear regime and a non-linear regime, which can be explained using simple dimensional arguments and balances of forces.[7]

Further interest in the flow studied in the current paper arises from the use of electromagnetic forcing in recent laboratory experiments to reproduce geophysical flows such as zonal jets in the atmosphere and the oceans.[8,9] One clear difference between such experiments and oceanic/atmospheric flows is the nature of the forcing. For example, surface ocean currents are mainly driven by wind stress—for which case the Ekman theory was actually developed—as opposed to a force acting on the whole fluid volume in the laboratory setups. This difference raises several questions. Are there any dynamical differences when a flow is driven by a non-conservative body force? Are the classical theories for rotating flows still applicable? Is the Ekman theory, in particular, still applicable? As we shall show here, even a simple non-conservative body force can have an important effect on the Ekman boundary layers. In particular, we draw attention to the fact that the value of the Rossby number does not determine solely the applicability of the Ekman theory in this case.

II. EXPERIMENTAL SETUP

The experimental setup, similar to the one described in Ref. 7, consists of a water tank with a base of 34×30 cm^2 that, in this case, is placed on top of a rotating table. The tank is filled with a salt (NaCl) solution with a concentration of 178 g/l (with a kinematic viscosity[10] $\nu = 1.50 \times 10^{-6}$ m^2 s^{-1} and a density $\rho = 1190$ kg m^{-3}) to a depth H and covered with a transparent perspex lid to avoid free-surface deformations (see Fig. 1). The depth of the fluid was varied for different experiments taking the values $H = 1.2$, 2.0, and 3.2 cm.

To force the flow, two titanium electrodes are placed along two opposite sides of the tank, and three 30×10 cm^2 rectangular magnets are placed 1.1 cm underneath the tank bottom. The magnitude of the magnetic field of each of these magnets is 0.023 T just above their center. The electrodes are placed in compartments that are connected to the measurement area of the tank by a system of thin horizontal slits through which the electric current can easily pass, but that isolates the chemical reaction products generated at the electrodes from the flow to be studied. As shown in Fig. 1(b), the magnet at the center has its north pole facing up, while the two side magnets have their north pole facing down. A constant electric current is applied through the fluid using a power supply with a precision of 10^{-2} A. Due to the interaction of the electric current and the magnetic

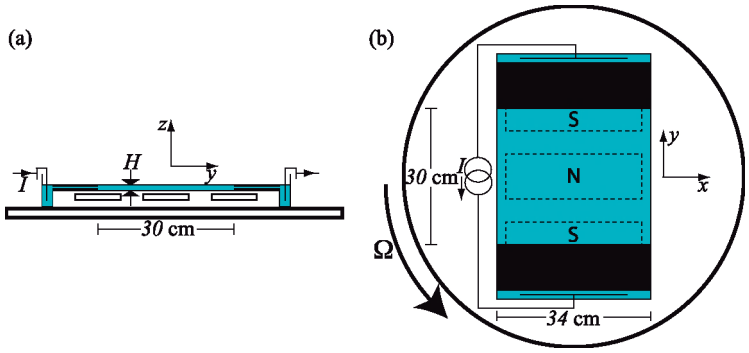

FIG. 1. Schematic representation of the experimental setup. (a) Vertical cross-section of the experimental setup. (b) Upper view of the experimental setup.

field of the magnets, a Lorentz force acting on the fluid is generated

$$\boldsymbol{F} = \boldsymbol{J} \times \boldsymbol{B}, \tag{1}$$

with $\boldsymbol{J}$ the current density, and $\boldsymbol{B}$ the magnetic field. For the experiments studied here, the induced current density and induced magnetic field are considered to be negligible. In other words, the current density $\boldsymbol{J}$ is only due to the injected electric current, and that magnetic field $\boldsymbol{B}$ is only due to the permanent magnets. This is a good approximation for these experiments as shown in Ref. 6.

For each experiment, the rotating table is set to a constant speed Ω until the fluid reaches solid-body rotation. Then, the electric current is switched on to start the forcing. The flow is then left to develop until it reaches a steady state. Particle image velocimetry (PIV) is used to measure the horizontal velocity field of the flow in a plane at mid-depth. To perform these measurements, the fluid was previously seeded with 106–150 μm polymethylmethacrylate particles which are illuminated at mid-depth with a laser sheet produced by a double-pulsed Nd:YAG laser mounted on the rotating table. Images of the central 34×28 cm^2 area of the tank are taken, using a Megaplus ES 1.0 camera, at different time intervals (ranging from 10 ms to 1.3 s) depending on the maximum velocity in the flow. These images are then cross-correlated using PIV software from PIVTEC GmbH, Göttingen, Germany to calculate the horizontal velocity field.

III. GOVERNING EQUATIONS AND NON-DIMENSIONAL PARAMETERS

A. Governing equations

We assume that the flow is governed by the Navier-Stokes equation which includes the Coriolis force and the Lorentz force,

$$\frac{\partial \boldsymbol{v}}{\partial t} + (\boldsymbol{v} \cdot \nabla)\boldsymbol{v} + 2\boldsymbol{\Omega} \times \boldsymbol{v} = -\frac{1}{\rho}\nabla P + \nu\nabla^2\boldsymbol{v} + \frac{1}{\rho}\boldsymbol{J} \times \boldsymbol{B}, \tag{2}$$

and by the continuity equation for an incompressible fluid,

$$\nabla \cdot \boldsymbol{v} = 0, \tag{3}$$

where $\boldsymbol{v}$ is the flow velocity, $\boldsymbol{\Omega} = (0, 0, \Omega)$ is the rotation vector of the system, and $P = p - \rho\Omega^2(x^2 + y^2)/2$ is the modified pressure.

For the interpretation of the results, it will be useful to also consider the vorticity equation

$$\frac{\partial \boldsymbol{\omega}}{\partial t} + [(\boldsymbol{v} \cdot \nabla)\boldsymbol{\omega} + (\boldsymbol{\omega} \cdot \nabla)\boldsymbol{u}] + 2(\boldsymbol{\Omega} \cdot \nabla)\boldsymbol{v} = \nu\nabla^2\boldsymbol{\omega} + \frac{1}{\rho}\nabla \times (\boldsymbol{J} \times \boldsymbol{B}), \tag{4}$$

which is obtained by taking the curl of Eq. (2).

B. Considerations on the Lorentz force

Whenever the current density $\boldsymbol{J}$ is spatially uniform, the Lorentz force given in Eq. (1) can be written as

$$\boldsymbol{F} = \boldsymbol{J} \times \boldsymbol{B} = \nabla(\boldsymbol{J} \cdot \boldsymbol{A}) - (\boldsymbol{J} \cdot \nabla)\boldsymbol{A}, \tag{5}$$

where $\boldsymbol{A}$ is the vector potential for $\boldsymbol{B}$ such that $\boldsymbol{B} = \nabla \times \boldsymbol{A}$. In addition, we have considered the Coulomb gauge $\nabla \cdot \boldsymbol{A} = 0$ without loss of generality.

The term $\nabla(\boldsymbol{J} \cdot \boldsymbol{A})$ in Eq. (5) can be absorbed in the pressure term of the Navier-Stokes equation (2), which then becomes

$$\frac{\partial \boldsymbol{v}}{\partial t} + (\boldsymbol{v} \cdot \nabla)\boldsymbol{v} + 2\boldsymbol{\Omega} \times \boldsymbol{v} = -\frac{1}{\rho}\nabla(P - \boldsymbol{J} \cdot \boldsymbol{A}) + \nu\nabla^2\boldsymbol{v} - \frac{1}{\rho}(\boldsymbol{J} \cdot \nabla)\boldsymbol{A}, \tag{6}$$

and it does not contribute to the generation of vorticity since $\nabla \times [\nabla(\boldsymbol{J} \cdot \boldsymbol{A})] = 0$. In other words, this term is a conservative contribution. Hence, vorticity is generated by the term $-(\boldsymbol{J} \cdot \nabla)\boldsymbol{A}$, which is divergence-free.

For a permanent magnet that is magnetized along the z-direction (as in the case considered in the current paper), $\boldsymbol{A}$ contains only horizontal components ($A_z = 0$) (see, e.g., Ref. 11). Since $\boldsymbol{J} = J\hat{\boldsymbol{j}}$ in our experiments, then $(\boldsymbol{J} \cdot \nabla)\boldsymbol{A} = J\partial\boldsymbol{A}/\partial y$ implying that vorticity is driven solely by the horizontal components of the Lorentz force. Furthermore, the Lorentz force term in the vorticity equation (4) can be simplified to

$$\nabla \times (\boldsymbol{J} \times \boldsymbol{B}) = J\frac{\partial \boldsymbol{B}}{\partial y}. \tag{7}$$

Since the velocity measurements are taken on a horizontal plane, we shall focus on the vertical component of the vorticity ω_z that, as seen in the previous equation, can be produced by the gradient in the y-direction of the vertical component of the magnetic field B_z.

In addition, the vertical component of the Navier-Stokes equation (2) can be written as

$$\frac{\partial v_z}{\partial t} + (\boldsymbol{v} \cdot \nabla)v_z = -\frac{1}{\rho}\frac{\partial P^*}{\partial z} + \nu\nabla^2 v_z, \tag{8}$$

where the term $\nabla(\boldsymbol{J} \cdot \boldsymbol{A})$ has been absorbed in the pressure gradient term, such that $P^* = p - \rho\Omega^2(x^2 + y^2)/2 - \boldsymbol{J} \cdot \boldsymbol{A}$. The governing Poisson equation for P^*

$$-\frac{1}{\rho}\nabla^2 P^* = \mathrm{Tr}(\epsilon^2) - \frac{1}{2}\boldsymbol{\omega}^2 - 2\boldsymbol{\Omega} \cdot \boldsymbol{\omega} \tag{9}$$

with ϵ the rate-of-strain tensor, is obtained by taking the divergence of Eq. (6) and assuming an incompressible fluid [Eq. (3)].

Equation (9) implies that the z-dependence in P^* is inherited from the z-dependence of $\boldsymbol{\omega}$ or ϵ. Without background rotation this source term is nonlinear in nature. With sufficiently strong background rotation, the term $-2\boldsymbol{\Omega} \cdot \boldsymbol{\omega} = -2\Omega\omega_z$ becomes dominant and is linear in nature leading to a different scaling of vertical flow (recirculation) than in the non-rotating case. This means that the Lorentz force does not drive vertical motions (i.e., recirculations and secondary flows); these are driven by a z-dependent pressure as for vortical flows that are not driven by a Lorentz force such as the ones discussed in Refs. 3 and 12.

Finally, we rewrite the Lorentz force [Eq. (1)] in terms of the components of the magnetic field for the particular experimental setup discussed in the current paper

$$\boldsymbol{F} = \boldsymbol{J} \times \boldsymbol{B} = J\left(\frac{\partial A_y}{\partial x} - \frac{\partial A_x}{\partial y}\right)\hat{\boldsymbol{\imath}} + J\frac{\partial A_y}{\partial z}\hat{\boldsymbol{k}} = JB_z\hat{\boldsymbol{\imath}} - JB_x\hat{\boldsymbol{k}}. \tag{10}$$

The magnitude of the Lorentz force driving the flow in the horizontal direction is characterized by $[JB_z] = IB/(L_xH)$, where $L_x = 34$ cm is the length of the tank along the electrodes; the brackets denote the order of magnitude; and I is the magnitude of the total electric current through the fluid. We define $B = \langle|B_z(x, y, H/2)|\rangle$ with $\langle\cdots\rangle$ the spatial average over the horizontal plane since the measurements are carried on the plane at half-depth. To calculate the spatial average of B_z, we

assume that the spatial distribution of the magnetic field is given by the analytical model described in the Appendix, and then, the magnitude is normalized using the measured value right on top of the center of the magnet. The Lorentz force term in the vertical direction, $JB_x\hat{\boldsymbol{k}}$ in Eq. (10), is absorbed by the pressure gradient as discussed before.

C. Non-dimensional parameters

Dimensional analysis shows that three independent dimensionless parameters can be defined as the control parameters of the problem. The Chandrasekhar number,

$$\mathrm{Ch} \equiv \frac{IBH}{\rho\nu^2}, \tag{11}$$

characterizes the electromagnetic forcing and represents the ratio of the Lorentz force to the viscous force. The Ekman number,

$$\mathrm{Ek} \equiv \frac{\nu}{\Omega H^2}, \tag{12}$$

characterizes the system's rotation rate and represents a ratio of the Coriolis force to viscous forces. The aspect ratio

$$\delta \equiv \frac{H}{L_x} \tag{13}$$

is a geometrical parameter that characterizes the shallowness of the flow. The horizontal length scales of the tank, which have a ratio $L_x/L_y = 1.13$, remain unchanged for all experiments since the study of their effect is outside the scope of the current paper.

In the current paper, we consider exclusively the case of a shallow layer ($\delta \ll 1$). This has two important implications: horizontal viscous dissipation is negligible with respect to vertical viscous dissipation particularly due to the boundary layers, and the magnitude of the magnetic field varies little within the fluid layer. In fact, for the deepest configuration the magnitude of the magnetic field above the center of the magnet just below the lid is 19% weaker than at the bottom of the tank; for the shallowest configuration the difference is only of 5%. For large values of δ, electromagnetically forced electrolytes can present richer dynamics, as observed in experiments on rotating turbulence using electromagnetic forcing.[13,14]

To characterize the response of the flow, we define the Reynolds number,

$$\mathrm{Re} \equiv \frac{UL_x}{\nu}, \tag{14}$$

which gives a ratio of inertia forces to viscous forces, with U being a typical velocity scale of the flow. In the current paper, $U = \langle|\overline{\boldsymbol{v}(t, x, y, z = H/2)}|\rangle$, where the upper bar denotes the time average, $|...|$ denotes magnitude, and $\langle\cdots\rangle$ denotes the average over the horizontal plane. The time average was computed from 28 image pairs taken after the flow reaches a steady state. This number of image pairs is large enough so that the value of Re does not vary if more images are taken into account. Note that the definition of U differs from that in Ref. 7, where only the velocity along the symmetry axis $y = 0$ was taken into account. In the current paper, the velocity over the entire measurement plane is used since the symmetry with respect to $y = 0$ may be broken due to background rotation.

The Rossby number Ro, which is also commonly used to characterize flows subjected to background rotation, can be obtained from a combination of the other parameters

$$\mathrm{Ro} \equiv \frac{U}{2\Omega L_x} = \frac{1}{2}\mathrm{ReEk}\delta^2. \tag{15}$$

The Rossby number represents a ratio of the convective acceleration to the Coriolis acceleration, and it is a response parameter as the Reynolds number.

IV. NUMERICAL SIMULATIONS

Numerical simulations were performed to obtain the three-dimensional velocity field of the flow, and particularly, the vertical profile of the horizontal velocity. The flows obtained in the laboratory experiments where reproduced by setting the fluid properties as in the experiments; defining the dimensions of the numerical domain equal to those of the tank; and applying no-slip boundary conditions. In addition, the simulations allowed us to explore regions of the parameter space that were outside the experimental limits by reaching higher forcing magnitudes (i.e., reaching higher Ch-values).

Equations (2) and (3) were solved using a finite difference code (COMSOL[15]). The domain was discretized using a mesh with 15 000 elements, which is equivalent to solve for approximately 350 000 degrees of freedom. In the horizontal a triangular mesh was used, while in the vertical a swept rectangular mesh with 10 levels was used. In this way, we obtain a good spatial resolution in both directions while keeping computational costs low. Both the spatial and temporal resolution were checked by increasing them until the solution converged.

The electromagnetic forcing was introduced in the simulations using the analytical model for the magnetic field described in the Appendix. Figure 2(a) shows the calculated distribution of the vertical component of the magnetic field at half-depth for a simulation with $\delta = 0.035$. In this figure, the three magnets are clearly distinguishable. In Fig. 2(b), $\partial B_z/\partial y$, the gradient in the y-direction of the vertical component of the magnetic field is plotted for the same plane. Figures 2(c) and 2(d) show the horizontal velocity and the vertical vorticity fields in the case without background rotation (Ek $= \infty$) from a numerical simulation with $\delta = 0.035$ and Ch $= 228$, while Figs. 2(e) and 2(f) show the same fields from an experiment with $\delta = 0.035$ and Ch $= 672$. As can be seen, from the velocity field, a dipolar flow structure is created with velocity in the positive x-direction above the central magnet and velocity in the negative x-direction above the side magnets. Furthermore, it can be seen

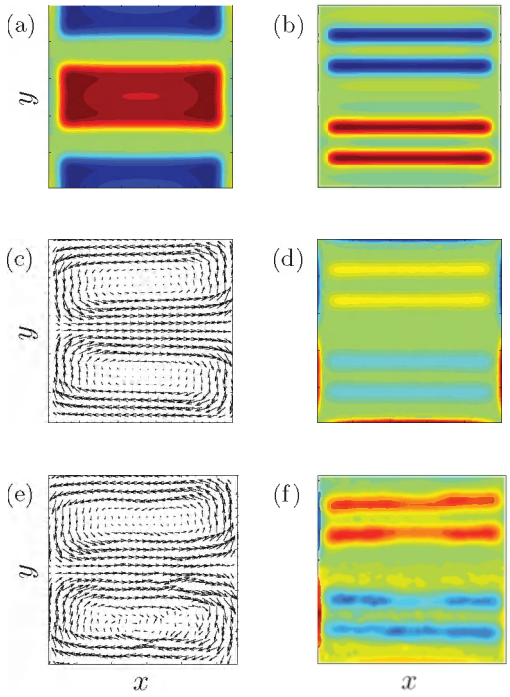

FIG. 2. Comparison of the analytically obtained magnetic field distribution with results from numerical simulations and laboratory experiments for low Ch-values. Analytically obtained distributions of (a) the vertical component of the magnetic field B_z and (b) of $\partial B_z/\partial y$. (c) Horizontal velocity and (d) vertical vorticity fields at half-depth for a numerical simulation with Ek $= \infty$, $\delta = 0.035$, and Ch $= 228$. (e) Horizontal velocity and (f) vertical vorticity fields at half-depth measured in a laboratory experiment with Ek $= \infty$, $\delta = 0.035$, and Ch $= 672$.

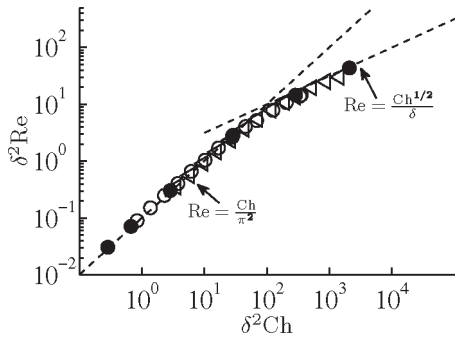

FIG. 3. Measured values of the Reynolds number Re as a function of the Chandrasekhar number Ch (the axes have been scaled with δ^2). Experimental results for Ek $= \infty$ and $\delta = 0.035$ (◯), and Ek $= \infty$ and $\delta = 0.059$ (◁). The filled circles (●) denote numerical results for Ek $= \infty$ and $\delta = 0.035$. The dashed lines represent the analytical scaling relations given by Eqs. (16) and (17).

that the vorticity distribution corresponds well with the spatial distribution of $-\partial B_z/\partial y$. However, this correspondence only exists for low Ch-values, as we shall show below in more detail.

V. THE CASE WITHOUT BACKGROUND ROTATION (Ek = ∞)

For the case of no background rotation, it has been previously shown[7] that there are two different scaling regimes

$$\mathrm{Re} \approx \mathrm{Ch}/\pi^2 \tag{16}$$

for weak forcing ($\delta^2\mathrm{Ch} \lesssim \pi^4$), and

$$\mathrm{Re} \approx \mathrm{Ch}^{1/2}/\delta \tag{17}$$

for strong forcing ($\delta^2\mathrm{Ch} \gtrsim \pi^4$). These results are clearly reproduced with the definitions of Re and Ch used in the current paper, as shown in Fig. 3. In this figure, we plot the obtained values of the Reynolds number Re as a function of the Chandrasekar number Ch for the case of no rotation (Ek $= \infty$) and two different values of the aspect ratio ($\delta \approx 0.035$ and 0.059). A collapse of the curves for both values of δ is observed when the axes are scaled by δ^2. In addition, there is a good agreement between experimental and numerical results.

In Ref. 7, it was argued using dimensional analysis that the transition between the two regimes could be explained by a change in the vertical profile of the horizontal velocity. This is here supported by the results from numerical simulations. Figure 4 shows the vertical profiles of the horizontal velocity averaged over time and on horizontal planes for two numerical simulations: one for $\delta^2 Ch \lesssim \pi^4$ [weak forcing, Fig. 4(a)] and one for $\delta^2 Ch \gtrsim \pi^4$ [strong forcing, Fig. 4(b)]. For weak forcing, the Poiseuille-like profile is clearly observed, while for strong forcing the flow consists of

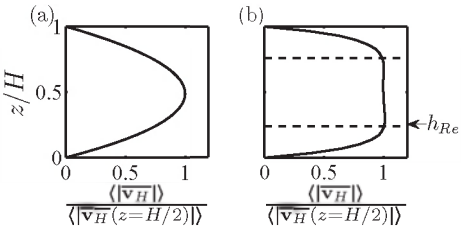

FIG. 4. Vertical profiles of the horizontal velocity obtained numerically from simulations with Ek $= \infty$, $\delta = 0.035$ (a) Ch $= 228$ and (b) Ch $= 1.66 \times 10^6$. $\boldsymbol{v}_H = (v_x, v_y, 0)$; the over-bar denotes the time average; and $\langle\cdots\rangle$ denotes spatial average of a horizontal plane. The vertical profile is normalized by the value of $\langle|\overline{\mathbf{v}_H}|\rangle$ at half-depth. The dashed lines in (b) denote the thickness of the boundary layers $z/H = h_{\mathrm{Re}} = \pi/(2\delta\mathrm{Re}^{1/2})$.

an inviscid interior and two boundary layers (one at the bottom and one at the top). The definition for the thickness of these boundary layers (as proposed in Ref. 7)

$$h_{\mathrm{Re}} \equiv \frac{\pi}{2\delta \mathrm{Re}^{1/2}} \tag{18}$$

gives a good estimate for the actual physical thickness of these boundary layers. The transition between the two regimes occurs when $h_{\mathrm{Re}} \approx 1/2$, and it is explained by the fact that inertia forces become dominant over viscous forces away from the upper and lower boundaries.

VI. THE CASE WITH BACKGROUND ROTATION

Figure 5 shows the response of the flow (given by $\mathrm{Re}\delta^2$) as a function of the forcing (given by $\delta^2\mathrm{Ch}$) for different experiments and numerical simulations with $\mathrm{Ek} = 3.5 \times 10^{-3}$. The experiments were carried out with three different aspect ratios $\delta = 0.035$, 0.058, and 0.094, while the simulations were performed for $\delta = 0.035$ and 0.094. It can be observed that there is similar behavior as in the non-rotating case in that there are two clear distinct scaling regimes, and that the curves for the same Ek-value but different δ-value collapse if both Re and Ch are scaled by δ^2.

To explain these regimes, we assume that, for this Ek-value, the damping in the interior is mainly due to the linear contribution to the vortex stretching induced by Ekman suction (see Ref. 16). This form of damping is commonly known as Ekman damping or Ekman friction. In other words, we assume that the most important contribution to viscous damping for the vertical component of the vorticity equation (4) is given by a term

$$-2\mathrm{Ek}^{1/2}\Omega\omega_z$$

and not by molecular viscous diffusion. The factor 2 in the Ekman damping term is included to account for the presence of both the bottom and top boundary layers.

We then presuppose a balance between Ekman friction and the Lorentz force, i.e.,

$$2\mathrm{Ek}^{1/2}\Omega U \sim \frac{IB}{\rho L_x H} \tag{19}$$

which yields

$$\mathrm{Re} \sim \frac{1}{2}\mathrm{Ek}^{1/2}\mathrm{Ch}. \tag{20}$$

This relationship is shown in Fig. 5, where it can be seen that this scaling relation agrees well with numerical and experimental results within the first regime.

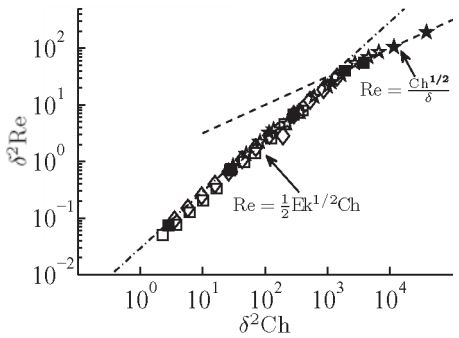

FIG. 5. Values of the Reynolds number Re as a function of the Chandrasekhar number Ch (the axes have been scaled with δ^2). Experimental results for $\mathrm{Ek} = 3.5 \times 10^{-3}$ and $\delta = 0.035$ (□), 0.054 (◊), and 0.094 (☆). The equivalent filled symbols denote numerical results for the same Ek and δ values. The dashed lines denote the analytical scaling relations given by Eqs. (20) and (22).

For strong forcing, we presuppose that there is a balance between convective acceleration and the Lorentz force, i.e.,

$$\frac{IB}{\rho L_x H} \sim \frac{U^2}{L_x} \tag{21}$$

which yields

$$\mathrm{Re} \sim \frac{\mathrm{Ch}^{1/2}}{\delta}, \tag{22}$$

as in the case of no background rotation. The relationship (22) is also shown in Fig. 5, which reveals a good agreement between this scaling relation and the experimental and numerical results for large values of $\delta^2\mathrm{Ch}$. Furthermore, Eqs. (20) and (22) give good estimates for the value of the Reynolds number.

We define a typical non-dimensional thickness h_{Ek} for the boundary layer in the rotating case. As for the case without background rotation, the boundary layers are said to exist if their thickness is smaller than half the total depth (i.e., if $h_{\mathrm{Ek}} < 1/2$). In this way,

$$h_{\mathrm{Ek}} \equiv \frac{\pi^2}{4}\mathrm{Ek}^{1/2}. \tag{23}$$

Note that the only difference with the typical definition of the Ekman boundary layer thickness is the prefactor $\pi^2/4$, which is added to fit the condition that the Ekman damping is equal to the one due to the Poisseuille-like profile at $h_{Ek} \approx 1/2$, i.e.,

$$\mathrm{Re} \approx \frac{\mathrm{Ch}}{\pi^2} \approx \frac{1}{2}\mathrm{Ek}^{1/2}\mathrm{Ch} \quad \text{for} \quad h_{\mathrm{Ek}} \approx \frac{1}{2}. \tag{24}$$

Clearly, in the case when a vertical Poiseuille-like profile exists over the whole depth, the Ekman theory and Eq. (20) do no longer hold since there are no Ekman boundary layers at all.

Figure 6 shows the response of the flow in terms of $\delta^2\mathrm{Re}\,\mathrm{Ek}^{1/2}/2$ as a function of $\delta^2\mathrm{Ch}\,\mathrm{Ek}/4$. In this figure, we have included the data previously shown in Fig. 5, a set of experiments with $\mathrm{Ek} = 3.5 \times 10^{-2}$, $\delta = 0.035$ and several Ch-values, a set of numerical results for simulations with $\mathrm{Ek} = 4.1 \times 10^{-2}$, $\delta = 0.035$ and different Ch-values, and a set of numerical results for simulations with $\mathrm{Ek} = 4.0 \times 10^{-2}$, $\delta = 0.018$ and different Ch-values. Due to the correct scaling of the axes, the curves for different Ek-values and δ-values collapse. Furthermore, the transition between the regimes occurs at $\delta^2\mathrm{Re}\,\mathrm{Ek}^{1/2}/2 \approx \delta^2\mathrm{Ch}\,\mathrm{Ek}/4 \approx 1$. This gives confidence in the validity of Eqs. (20) and (22) for different Ek-values up to $\mathrm{Ek} \approx 4/\pi^4$ ($h_{\mathrm{Ek}} \approx 1/2$).

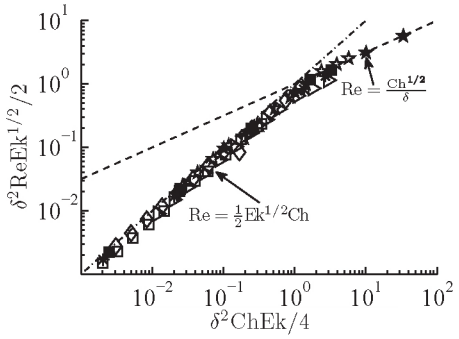

FIG. 6. Response of the flow given by the parameter $\delta^2\mathrm{Re}\,\mathrm{Ek}^{1/2}/2$ as a function of the control parameter $\delta^2\mathrm{Ch}\,\mathrm{Ek}/4$ for laboratory experiments and numerical simulations with different values of Ek, Ch, and δ. The markers denote the same experimental and numerical results as in Fig. 5 with the addition of experiments with $\mathrm{Ek} = 3.5 \times 10^{-2}$, $\delta = 0.035$, and several Ch-values (▷); numerical simulations with $\mathrm{Ek} = 4.1 \times 10^{-2}$, $\delta = 0.035$ and several Ch-values (+); and numerical simulations with $\mathrm{Ek} = 4.0 \times 10^{-2}$, $\delta = 0.018$ and several Ch-values (*). The dashed lines represent the scaling relations (20) and (22).

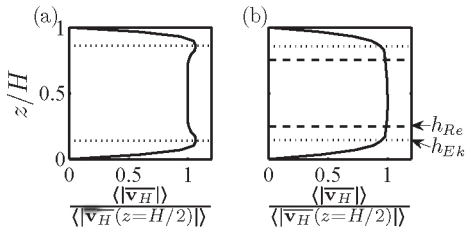

FIG. 7. Vertical profiles of horizontal velocity obtained numerically for two simulations: (a) Ch = 228 and (b) Ch = 1.66×10^6, Ek = 3.5×10^{-3}, $\delta = 0.035$. $\boldsymbol{v}_H = (v_x, v_y, 0)$; the over-bar denotes the time average; and $\langle \cdots \rangle$ denotes spatial average over a horizontal plane. The vertical profile is normalized by the value of $\langle|\overline{\mathbf{v}_H}|\rangle$ at half-depth. The dashed lines denote the thickness of the boundary layers given by $z/H = h_{\mathrm{Re}}$, and the dotted line denotes the thickness of the boundary layer given by $z/H = h_{\mathrm{Ek}}$.

Figure 7 shows the vertical profile of the horizontal velocity for two different simulations with $\mathrm{Ek} = 3.5 \times 10^{-3}$. The same Ch and δ values as in Fig. 4 for the case without background rotation have been used. For Ch = 228 [Fig. 7(a)], we observe the typical profile for flows subjected to strong rotation composed of a geostrophic interior where $\partial \boldsymbol{v}/\partial z \approx 0$ and two Ekman boundary layers which are characterized by the velocity maximum at $z/H \approx h_{\mathrm{Ek}}$. On the other hand, for $\mathrm{Ch} = 1.66 \times 10^6$ [Fig. 7(b)], the typical profile with the Ekman boundary layers is lost and a profile similar to that shown in Fig. 4(b) for the case of zero background rotation and strong forcing is recovered. Furthermore, we observe in Fig. 7(b) that the thickness of the Ekman boundary layers h_{Ek} is close to that for the non-rotating case h_{Re}. However, $h_{\mathrm{Re}} > h_{\mathrm{Ek}}$, which suggests that the transition does not occur when h_{Re} becomes smaller than h_{Ek} as for decaying vortices.[3]

The transition between the two regimes can be obtained by the intersection of the two lines given by Eqs. (20) and (22), which occurs when

$$\frac{1}{2}\mathrm{Ek}^{1/2}\mathrm{Ch} \approx \frac{\mathrm{Ch}^{1/2}}{\delta}. \tag{25}$$

For the non-rotating case, the transition between the two regimes can be explained by the dominance of inertia forces over viscous forces in the nonlinear regime. However, the physical explanation for the case of strong rotation, which depends on the parameter

$$\Pi_1 \equiv \frac{1}{4}\delta^2 \mathrm{Ch}\,\mathrm{Ek} \approx \frac{IBH}{4\rho L_x^2 \nu \Omega}, \tag{26}$$

is more complex since the magnitude of the forcing, viscosity, and the rotation rate must all be taken into account. The condition for the applicability of the linear Ekman theory is then

$$\Pi_1 = \frac{1}{4}\delta^2 \mathrm{Ch}\,\mathrm{Ek} \lesssim 1 \tag{27}$$

provided that also $h_{\mathrm{Ek}} \lesssim 1/2$ [i.e., $\mathrm{Ek} \lesssim 4/\pi^4 \approx 4.1 \times 10^{-2}$]. An equivalent condition can be expressed in terms of the response parameters of the problem (Re and Ro)

$$\Pi_2 \equiv \frac{\mathrm{Ro}}{\mathrm{Ek}^{1/2}} = \frac{1}{2}\delta^2 \mathrm{Re}\mathrm{Ek}^{1/2} = \frac{U\nu^{1/2}}{\Omega^{3/2} L_x H} \lesssim 1. \tag{28}$$

The dependence of the transition on Π_1 clearly indicates that the presence of a non-conservative body force is critical for the applicability of the Ekman boundary layer theory. Furthermore, the limit for the applicability of the Ekman boundary layer theory does not depend exclusively on the Rossby number as for flows without a body force. This means that the transition is not due to convective acceleration becoming dominant over the Coriolis force. Actually, since the critical Rossby number at which the transition occurs decreases with the square root of the Ekman number, the transition can occur already for $\mathrm{Ro} \ll 1$.

To further understand the physical meaning of the transition between the two regimes, we consider the vertical component of the vorticity equation (4)

$$(\boldsymbol{v}\cdot\nabla)\omega_z + 2[(\boldsymbol{\Omega}\cdot\nabla)\boldsymbol{v}]\cdot\hat{\boldsymbol{k}} = -2\mathrm{Ek}^{1/2}\Omega\omega_z + \frac{J}{\rho}\frac{\partial B_z}{\partial y}, \tag{29}$$

where we have made the following assumptions: the flow is steady; horizontal viscous diffusion is negligible with respect to Ekman friction; and vortex stretching is only due to Ekman pumping.

We define the non-dimensional variables (denoted by primes)

$$\boldsymbol{v} = U\boldsymbol{v}', \qquad \omega_z = \frac{U}{L_x}\omega_z', \qquad \nabla = \frac{1}{L_x}\nabla', \qquad B_z = B_z'.$$

These variables are substituted into Eq. (29) to obtain the non-dimensional equation

$$\mathrm{Ro}(\boldsymbol{v}'\cdot\nabla')\omega_z' + [(\hat{\boldsymbol{k}}\cdot\nabla')\boldsymbol{v}']\cdot\hat{\boldsymbol{k}} = -\mathrm{Ek}^{1/2}\omega_z' + \frac{\mathrm{Ch}\,\mathrm{Ek}}{2\mathrm{Re}}\frac{\partial B_z'}{\partial y'}. \tag{30}$$

Substituting the scaling for the Reynolds number in the regime of weak forcing and strong rotation $\mathrm{Re} = \mathrm{Ek}^{1/2}\mathrm{Ch}/2$ into Eq. (30), yields

$$\frac{1}{4}\mathrm{Ek}\,\mathrm{Ch}\,\delta^2(\boldsymbol{v}'\cdot\nabla')\omega_z' + \frac{1}{\mathrm{Ek}^{1/2}}[(\hat{\boldsymbol{k}}\cdot\nabla')\boldsymbol{v}']\cdot\hat{\boldsymbol{k}} = -\omega_z' + \frac{\partial B_z'}{\partial y'}. \tag{31}$$

In this equation, the non-dimensional parameter Π_1 is recovered in front of the convective acceleration term. On the other hand, both Ekman friction and the forcing are of order unity. This implies that the magnitude of the convective acceleration with respect to these two terms will grow as Π_1. However, the relative magnitude of the Coriolis force with respect to the same two terms will grow as $\mathrm{Ek}^{-1/2}$.

Equation (29) can also be written in terms of the Rossby number

$$\frac{\mathrm{Ro}}{\mathrm{Ek}^{1/2}}(\boldsymbol{v}'\cdot\nabla')\omega_z' + \frac{1}{\mathrm{Ek}^{1/2}}(\hat{\boldsymbol{k}}\cdot\nabla'\boldsymbol{v}')\cdot\hat{\boldsymbol{k}} = -\omega_z' + \frac{\partial B_z'}{\partial y'}. \tag{32}$$

From this equation, it can be seen that the magnitude of the convective acceleration with respect to that of the Ekman friction and the electromagnetic forcing increases with $\mathrm{Ro}\,\mathrm{Ek}^{-1/2}$. Furthermore, the ratio between the magnitude of the convective acceleration and the magnitude of the Coriolis acceleration is given, as expected, by the Rossby number Ro.

VII. CYCLONE/ANTICYCLONE ASYMMETRY AND THE ROLE OF THE ROSSBY NUMBER

A typical characteristic of flows subjected to background rotation is the emergence of an asymmetry between cyclones and anticyclones. This can, for example, be due to differences in the stability of the vortices (see, e.g., Ref. 17) or due to nonlinear Ekman effects (see, e.g., Ref. 18). In the experiments discussed in the current paper, a cyclone/anticyclone asymmetry is observed for certain values of the parameters of the problem if the flow is subjected to background rotation. Figure 8 shows the vorticity field for three different experiments with the same value of Ek and δ ($\mathrm{Ek} = 3.5\times10^{-2}$, $\delta = 0.035$), and three different Ch-values. As can be seen, the symmetry between the cyclone and anticyclone is broken for the larger values of Ch. The asymmetry observed is characterized by a strong and compact anticyclone and a weak and enlarged cyclone, which can be explained by the asymmetric nature of the Ekman pumping as the Rossby number approaches unity.[18]

To quantify the cyclone/anticyclone asymmetry in the flow, we consider the probability distribution for the vertical component of the vorticity $P(\omega_z)$, and we define the quantity

$$S = \int |P(\omega_z) - P(-\omega_z)|d\omega_z, \tag{33}$$

such that $S = 0$ if the probability distribution is perfectly symmetric, and S increases if an asymmetry develops.

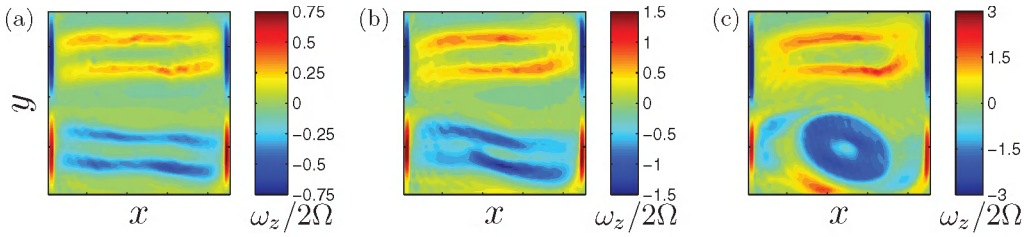

FIG. 8. Vertical vorticity field for three different experiments with Ek $= 3.5 \times 10^{-2}$, $\delta = 0.035$, and (a) Ch $= 4.95 \times 10^3$, (b) Ch $= 1.35 \times 10^4$, (c) Ch $= 3.67 \times 10^4$. The color denotes the value of the non-dimensional vertical vorticity: $\omega_z/2\Omega$.

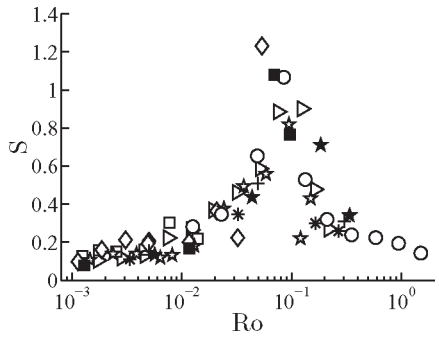

FIG. 9. Cyclone/anticyclone asymmetry as given by S as a function of the Rossby number Ro. The markers denote the same experimental results and numerical results as in Fig. 5. Additional data correspond to experiments with Ch $= 2.94 \times 10^5$, $\delta = 0.035$, and several Ek-values (◯).

Figure 9 shows the value of S as a function of the Rossby number for the same experiments and numerical simulations presented in Fig. 6 plus an additional set of experiments where the Ch-value is kept fix at Ch $= 2.94 \times 10^5$, $\delta = 0.035$, and the value of Ek is varied. As can be seen, the value of S exhibits a similar behavior for the different simulations and experiments when it is plotted as a function of the Rossby number. In particular, we can observe that as the value of Ro reaches Ro $\approx 10^{-2}$, the value of S sharply increases until it reaches a maximum at around Ro $\approx 10^{-1}$. Then, the asymmetry decreases as the Coriolis force starts to become negligible.

Even though the value of Ro governs the asymmetry in the flow, the value at which the asymmetry attains its maximum is still one order of magnitude smaller than unity (as seen in Fig. 9). This is due to the fact that the asymmetry arises locally when $|\omega_z/2\Omega| \approx 1$. This can be observed in Fig. 8 where it is precisely when $|\omega_z/2\Omega| \approx 1$ in the regions of high vorticity along the edges of the magnets that the asymmetry starts to be observed. The asymmetry occurs when the Rossby number Ro, as defined in Eq. (15) using the average horizontal velocity magnitude over the whole plane at mid-depth, is much smaller than unity because there are large regions where $\omega_z \approx 0$.

VIII. CONCLUSIONS

We have studied numerically and experimentally the response of a generic shallow flow to a non-conservative body force (electromagnetic forcing in an electrolyte) and to background rotation. We have shown that two scaling regimes—a linear and a nonlinear regime—exist for the Reynolds number (flow velocity) as a function of the Chandrasekhar number (forcing magnitude) independently of the rotation rate.

For sufficiently strong rotation (Ek $\lesssim 4/\pi^2$), the linear Ekman theory is only applicable within the linear regime and the transition between the two regimes depends on the value of the parameter $\Pi_1 = \delta^2 \mathrm{Ch}\,\mathrm{Ek}/4$. This dependence clearly indicates that the limit for the applicability of the Ekman theory is affected by the presence of a non-conservative body force, and that it does not depend exclusively on the value of the Rossby number Ro (i.e., on the relative magnitude of convective

acceleration with respect to the Coriolis acceleration) as in decaying flows. In the experiments and simulations reported here, the Rossby number does, however, govern the appearance and magnitude of a cyclone/anticyclone asymmetry.

The previous conclusions have important implications for laboratory experiments on electromagnetically forced flows subjected to background rotation, in that having a small Rossby does not guarantee that the Ekman layer theory is applicable. However, according to the values presented in previous experimental work on flows of electrolytes forced electromagnetically and subjected to background rotation,[9] these experiments are within the regimes where the Ekman boundary layer theory is applicable.

The flow studied in the current paper exhibits an important similarity between the case with strong background rotation and the case without rotation: the existence of the linear and the nonlinear scaling regimes. Furthermore, it is possible to describe a generic physical explanation for such behavior in both cases. First, in the linear regime convective acceleration is negligible with respect to the viscous damping and the forcing. The transition between the two regimes occurs when nonlinear effects become of the same order as the viscous damping. This transition translates into the modification of the vertical profile through advection and a resulting increase in viscous dissipation. In this way, the mean flow tends towards a steady state even for large Re-values.

APPENDIX: SPATIAL STRUCTURE OF THE MAGNETIC FIELD

The relevant equations to compute the magnetic field of the permanent magnet are

$$\nabla \cdot \boldsymbol{B} = 0, \tag{A1}$$

$$\nabla \times \boldsymbol{H} = \boldsymbol{J}_{free} = 0 \quad \rightarrow \quad \boldsymbol{H} = -\nabla \Phi, \tag{A2}$$

$$\boldsymbol{B} = \mu_0(\boldsymbol{H} + \boldsymbol{M}), \tag{A3}$$

with ϕ the magnetic potential, μ_0 the magnetic permeability, $\boldsymbol{H}$ is the magnetic field strength, and $\boldsymbol{M}$ the magnetization.

We consider a rectangular magnet with thickness d and sides $2L_m$ and $6L_m$which is uniformly magnetized in the z-direction, such that

$$\boldsymbol{M} = M_0\hat{\boldsymbol{k}} \quad \text{for} \quad |x| < 3L_m, |y| < L_m \quad \text{and} - d < z < 0 \tag{A4}$$

with M_0 the magnitude of the magnetization.

From now on, we will use the following dimensionless variables denoted by a tilde:

$$(\tilde{x}, \tilde{y}, \tilde{z}) = \frac{1}{L_m}(x, y, z), \quad \tilde{\Phi} = \frac{\Phi}{L_m M_0}, \quad \tilde{\boldsymbol{M}} = \frac{\boldsymbol{M}}{M_0}, \quad \tilde{\boldsymbol{B}} = \frac{\boldsymbol{B}}{\mu_0 M_0} = \frac{\boldsymbol{B}}{B_0}, \quad \tilde{\eta} = \frac{d}{L} \tag{A5}$$

with $B_0 = \mu_0 M_0$ as the typical magnitude of the magnetic field. From now on, the tildes will be omitted to simplify the notation.

Combining Eqs. (A1)–(A3) results in a Poisson equation for the magnetic potential

$$\nabla^2\Phi = \nabla \cdot \boldsymbol{M} = \begin{cases} \delta_D(z+\eta) - \delta_D(z) & \text{for} \quad |x| < 3 \cap |y| < 1 \\ 0 & \text{for} \quad |x| > 3 \cup |y| > 1 \end{cases}, \tag{A6}$$

where δ_D is the Dirac delta function, and $\boldsymbol{M} = \hat{\boldsymbol{k}}$, for $|x| < 3$, $|y| < 1$, and $-\eta < z < 0$. The solution to Eq. (A6) is given in terms of Green's function for the Laplace operator and found to be given by

$$\Phi(x, y, z) = F(x, y, z) - F(x, y, z+\eta) \tag{A7}$$

with

$$F(x, y, z) = \frac{1}{4\pi}\int_{x-3}^{x+3} d\kappa \int_{y-1}^{y+1} \xi \frac{1}{\sqrt{\kappa^2 + \xi^2 + z^2}}, \tag{A8}$$

from which the solution for the magnetic field in the x and y directions easily follows. However, here we shall not develop the solution for B_y, the magnetic field in the y-direction, since it is parallel to the electric current and does not contribute to the forcing. To calculate B_x, the magnetic field in the x-direction, we first integrate (A8) with respect to ξ, so that

$$F(x,y,z)=\frac{1}{4\pi}\int_{x-3}^{x+3}d\kappa[\ln(y+1+\sqrt{\kappa^2+(y+1)^2+z^2})$$
$$-\ln(y-1+\sqrt{\kappa^2+(y-1)^2+z^2})] \tag{A9}$$

and

$$\begin{aligned}B_x=-\frac{\partial\Phi}{\partial x}=&P(x+3,y+1,z+\eta)-P(x+3,y-1,z+\eta)\\&+P(x-3,y-1,z+\eta)-P(x-3,y+1,z+\eta)\\&-P(x+3,y+1,z)+P(x+3,y-1,z)\\&-P(x-3,y-1,z)+P(x-3,y+1,z)\end{aligned} \tag{A10}$$

with

$$P(x,y,z)=\frac{1}{4\pi}\ln(y+\sqrt{x^2+y^2+z^2}). \tag{A11}$$

To calculate B_z, the magnitude of the magnetic field in the z-direction,

$$\frac{\partial F}{\partial z}=\frac{1}{4\pi}\int_{x-3}^{x+3}d\kappa\left(\frac{1}{y+1+\sqrt{\kappa^2+(y+1)^2+z^2}}\times\frac{z}{\sqrt{\kappa^2+(y+1)^2+z^2}}\right.$$
$$\left.-\frac{1}{y-1+\sqrt{\kappa^2+(y-1)^2+z^2}}\times\frac{z}{\sqrt{\kappa^2+(y-1)^2+z^2}}\right), \tag{A12}$$

which yields after integration

$$\frac{\partial F}{\partial z}=W(x+3,y+1,z)-W(x-3,y+1,z) \tag{A13}$$

with

$$W(x,y,z)=\frac{1}{2\pi}\arctan\left(\frac{\sqrt{y^2+z^2}-y}{z}\times\frac{\sqrt{x^2+y^2+z^2}-\sqrt{y^2+z^2}}{x}\right).$$

Finally, the magnitude of the magnetic field in the z-direction for the rectangular magnet considered is given by

$$\begin{aligned}B_z=&W(x+3,y+1,z+\eta)-W(x-3,y+1,z+\eta)\\&-W(x+3,y-1,z+\eta)+W(x-3,y-1,z+\eta)\\&-W(x+3,y+1,z)+W(x-3,y+1,z)\\&+W(x+3,y-1,z)-W(x-3,y-1,z).\end{aligned} \tag{A14}$$

[1] H. P. Greenspan, *The Theory of Rotating Fluids* (Cambridge University Press, Cambridge, 1968), p. 327.
[2] V. W. Ekman, "On the influence of the Earth's rotation on ocean currents," Ark. Mat., Astron. Fys. **2**, 1–52 (1905).
[3] M. Duran-Matute, L. P. J. Kamp, R. R. Trieling, and G. J. F. van Heijst, "Regimes of two-dimensionality of decaying shallow axisymmetric swirl flows with background rotation," J. Fluid Mech. **691**, 214–244 (2012).
[4] E. M. King, S. Stellmach, J. Noir, U. Hansen, and J. M. Aurnou, "Boundary layer control of rotating convection systems" Nature (London) **457**, 301–304 (2009).
[5] R. P. J. Kunnen, R. J. A. M. Stevens, J. Overkamp, C. Sun, G. J. F. van Heijst, and H. J. H. Clercx, "The role of Stewartson and Ekman layers in turbulent rotating Rayleigh-Bénard convection," J. Fluid Mech. **688**, 422–442 (2011).

[6] A. Figueroa, F. Demiaux, S. Cuevas, and E. Ramos, "Electrically driven vortices in a weak dipolar magnetic field in a shallow electrolytic layer," J. Fluid Mech. **641**, 245 (2009).
[7] M. Duran-Matute, R. R. Trieling, and G. J. F. van Heijst, "Scaling and asymmetry in an electromagnetically forced dipolar flow structure," Phys. Rev. E **83**, 1–6 (2011).
[8] Y. Afanasyev and J. Wells, "Quasi-two-dimensional turbulence on the polar beta-plane: laboratory experiments," Geophys. Astrophys. Fluid Dyn. **99**, 1–17 (2005).
[9] S. Espa, G. Di Nitto, and A. Cenedese, "Laboratory study of forced rotating shallow water turbulence," J. Phys.: Conf. Ser. **318**, 082020 (2011).
[10] The kinematic viscosity was measured for the solution used in the experiments at the working temperature of 21°C using a capillary viscometer 501 13 from Schott Instruments.
[11] D. J. Griffiths, *An Introduction to Electrodynamics* (Prentice Hall, Upper Saddle River, 1999), p. 576.
[12] L. P. J. Kamp, "Strain-vorticity induced secondary motion in shallow flows," Phys. Fluids **24**, 023601 (2012).
[13] L. J. A. van Bokhoven, H. J. H. Clercx, G. J. F. van Heijst, and R. R. Trieling, "Experiments on rapidly rotating turbulent flows," Phys. Fluids **21**, 096601 (2009).
[14] L. Del Castello and H. J. H. Clercx, "Lagrangian velocity autocorrelations in statistically steady rotating turbulence," Phys. Rev. E **83**, 056316 (2011).
[15] "COMSOL 3.5 User's Guide," S. COMSOL AB, Stockholm.
[16] J. Pedlosky, *Geophysical Fluid Dynamics* (Springer, New York, 1982), p. 624.
[17] R. Kloosterziel and G. J. F. van Heijst, "An experimental study of unstable barotropic vortices in a rotating fluid," J. Fluid Mech. **223**, 1–24 (1991).
[18] L. Z. Sansón and G. J. F. van Heijst, "Nonlinear Ekman effects in rotating barotropic flows," J. Fluid Mech. **412**, 75–91 (2000).